

Article

Design Optimization of Tubular Heat Exchangers for a Free-Piston Stirling Engine Based on Improved Quasi-Steady Flow Thermodynamic Model Predictions

Dong-Jun Kim ¹, Yeongchae Park ¹, Tae Young Kim ^{2,*} and Kyuho Sim ^{1,*} 

¹ Department of Mechanical System Design Engineering, Seoul National University of Science and Technology, Seoul 01811, Korea; djkim@seoultech.ac.kr (D.-J.K.); newpark711@gmail.com (Y.P.)

² Department of Mechanical and Automotive Engineering, Seoul National University of Science and Technology, Seoul 01811, Korea

* Correspondence: tykim@seoultech.ac.kr (T.Y.K.); khsim@seoultech.ac.kr (K.S.)

Abstract: This paper presents the design optimization of a heat exchanger for a free-piston Stirling engine (FPSE) through an improved quasi-steady flow (iQSF) model and a central composite design. To optimize the tubular hot heat exchanger (HHX) design, a design set of central composite designs for the design factors of the HHX was constructed and the brake power and efficiency were predicted through the iQSF model. The iQSF model is improved because it adds various heat and power losses based on the QSF model and applies a heat transfer model that simulates the oscillating flow condition of an actual Stirling engine. Based on experimental results from the RE-1000, an FPSE developed by Sunpower, the iQSF model significantly improves the prediction error of the indicated power from 66.9 to 24.9% compared to the existing QSF model. For design optimization of the HHX, the inner diameter and the number of tubes with the highest brake power and efficiency were determined using a regression model, and the tube length was determined using the iQSF model. Finally, the brake output and efficiency of FPSE with the optimized HHX were predicted to be 7.4 kW and 36.4%, respectively, through the iQSF analysis results.

Keywords: free-piston Stirling engine; improved quasi-steady flow model; design of experiments; heat exchanger



Citation: Kim, D.-J.; Park, Y.; Kim, T.Y.; Sim, K. Design Optimization of Tubular Heat Exchangers for a Free-Piston Stirling Engine Based on Improved Quasi-Steady Flow Thermodynamic Model Predictions. *Energies* **2022**, *15*, 3326. <https://doi.org/10.3390/en15093326>

Academic Editors: Hassen M. Ouakad and Issam M. Bahadur

Received: 18 March 2022

Accepted: 27 April 2022

Published: 3 May 2022

Publisher's Note: MDPI stays neutral with regard to jurisdictional claims in published maps and institutional affiliations.



Copyright: © 2022 by the authors. Licensee MDPI, Basel, Switzerland. This article is an open access article distributed under the terms and conditions of the Creative Commons Attribution (CC BY) license (<https://creativecommons.org/licenses/by/4.0/>).

1. Introduction

Due to increasing concerns about the excessive use of fossil fuels, air pollution, and global warming, environmental regulations imposed on conventional heat engines are becoming increasingly stringent. Increasing population trends and more modern lifestyles worldwide are, however, demanding higher levels of energy. To meet these conflicting demands, the European Union (EU) took the initiative to raise the ratio of renewable energy usage beyond 20% out of the total energy consumption by 2020 by setting up the EU 2009 renewable energy action plan [1].

The Stirling engine is an external combustion engine that operates on a closed cycle. It consists of two isochoric heating/cooling and two isothermal compression/expansion processes based on the Stirling cycle.

The most important advantage of the Stirling engine is that it can use any type of heat source for fuel. Owing to this advantage, the Stirling engine can produce electricity using eco-friendly thermal energy sources such as biogas, biomass, and waste heat. In particular, the free-piston Stirling engine (FPSE), first proposed by Beale [2,3], replaces the slider-crank mechanism of the mechanical Stirling engine with a spring connected to the pistons. By reducing both the engine weight and the mechanical friction, it has a semi-permanent lifespan, leading to technological advances in the Stirling engine.

The Stirling engine consists of two types of parts; the first type is the moving parts, the displacer and power piston linked to the spring/load, and the second consists of the thermal energy transfer parts, specifically the hot heat exchanger, the regenerator, and the cold heat exchanger. The flow of the working fluid is induced between two enclosed spaces by the reciprocating motion of the displacer. While passing through the heat exchangers and regenerator, the temperature of the working fluid changes. The compression and expansion of the working fluid led by the temperature change result in the reciprocating motion of the power piston and, consequently, mechanical power.

Stirling engine analysis models for predicting performance outcomes have been developed by various researchers, and Dyson [4] classified Stirling engine analysis models into five major categories.

The zeroth-order model, first proposed by Beale [5], is an analysis model that introduces Beale's number, which predicts engine performance outcomes through correlations between operating conditions and performance based on experimental data of commercial engines. This model is the simplest, but the performance prediction accuracy is quite low.

The first-order model is an isothermal model that was initially proposed by Schmidt [6]. The isothermal model assumes that each space of the engine is isothermal; it calculates the volume and pressure of the engine space based on the ideal gas state equation and then predicts the pressure-volume (PV) power. Performance predictions by this model remain limited due to the isothermal assumption of the idealized engine space, but this type is widely used by those who design initial engines due to its simplicity.

The second-order model is an adiabatic model first proposed by Finkelstein [7] and Urieli [8]. The adiabatic model divides the engine space into two working spaces (compression space and expansion space) and three heat exchanger spaces (cooler, regenerator, and heater) and assumes that the working and heat exchanger spaces are adiabatic and isothermal, respectively. Each space defines a thermodynamic state quantity based on the energy equation and predicts the engine performance by numerical integration according to the time change. In particular, the non-ideal adiabatic model proposed by Urieli [8] is a quasi-steady flow (QSF) model that predicts heat transfer characteristics by assuming the flow in the heat exchanger as a steady-state flow. It is combined with various loss models [9–11] for reasonable performance predictions. It is widely used in optimization research due to its advantages of accuracy and fast analysis speeds. Based on these advantages, studies of various second-order models have recently been conducted [12,13].

Third-order models use the finite difference method to predict engine performance outcomes numerically by dividing the engine space into several connected one-dimensional nodes, defining each node using a differential equation that follows the laws of conservation of energy and conservation of mass. This model was performed by Finkelstein [14], Urieli [15], and Berchowitz [16]. In particular, Gedeon developed Sage [17–19], a program dedicated to the Stirling cycle based on the third-order model.

A fourth-order analysis refers to a model that divides and analyzes the engine space into multidimensional microspaces using computational fluid dynamics (CFD). It was studied by Mahkamov [20], Tew [21], and Wilson [22]. This model provides detailed analysis results of factors such as the flow velocity, flow pattern, temperature, and pressure distribution of the working fluid inside the engine. Despite these advantages, a disadvantage is that it requires a new model design each time depending on the engine shape. It also requires long calculation times for the analysis.

This study presents the design optimization of tubular heat exchangers of the FPSE developed by Nexergy lab at Seoultech [23] using the iQSF model and the development and verification of the iQSF model. The iQSF model is based on the second-order QSF model, and the third-order model is applied to the regenerator space, which is divided into several one-dimensional nodes. The model is verified through the experimental results of the RE-1000 engine developed by NASA's Lewis Research Center [24]. The optimized design of the heat exchanger also targets the engine developed by this institution. The optimized design of the heat exchanger aims to increase performance outcomes by reducing losses.

The design parameters of the heat exchanger are the tube diameter, length, and number of tubes. Each simulation case was determined from the design of experiment (DOE), which is a rapid and efficient method for determining the effects of variables [25]. The simulation results were fitted with a regression model [26], and the effects of the design variables were studied. The optimized design variables of the heat exchanger, which exhibited good performance and low losses, were obtained.

2. Description of the Developed FPSE

Figure 1 shows a cross-sectional view of a 3 kW FPSE design developed by Nexergy lab at Seoultech [27]. This engine was developed to use the exhaust gas waste heat below 500 °C from a 100 kW diesel generator as a heat source. The hot heat exchanger (HHX) and cold heat exchanger (CHX) are the shell-tube types, and 600 tubes with an inner diameter of 1.7 mm are applied to maximize the heat exchange area. However, using too many tubes will likely lead to welding defects, and in fact, many welding defects occurred here. Therefore, in this study, instead of the existing shell-tube type HHX, a tube-type HHX with dozens of tubes is used, and the design of the HHX tubes is optimized. In addition, the heat source temperature is increased to 600 °C to increase the engine performance. Table 1 presents the design parameters of the developed FPSE.

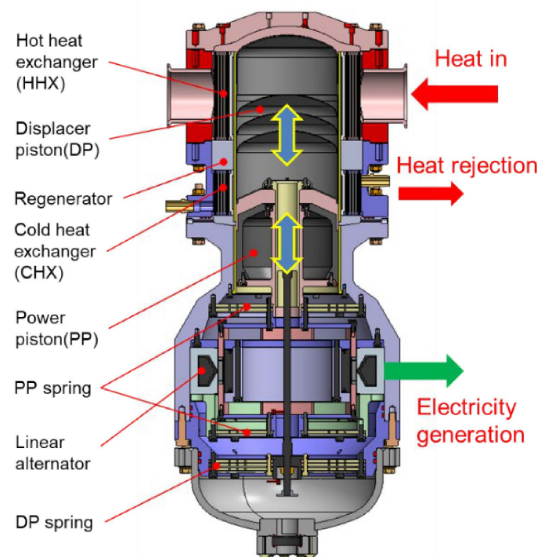


Figure 1. Cross-sectional view of a 3 kW FPSE design developed by Nexergy lab at Seoultech.

Table 1. Design parameters of the FPSE.

Parameter	Value	Unit	
Operating conditions	Working gas	Helium	
	Charge pressure	22	bar
	Heater wall temp.	600	°C
	Cooler reject temp.	25	°C
	Operating frequency	52	Hz
	DP and PP amplitude	11.6	mm
Heat exchanger geometry	Number of CHX tubes	600	ea.
	Inner diameter of CHX tubes	1.75	mm
	Length of the CHX tube	75	mm
Regenerator geometry	Regenerator type	Woven mesh	
	Fiber diameter	150	μM
	Porosity	88	%
Working space geometry	Expansion space length	15	mm
	Compression space length	25	mm

Table 1. Cont.

	Parameter	Value	Unit
Driving part geometry	PP and DP diameter	170	mm
	DP rod diameter	40	mm
	DP-liner clearance	140	μM
	PP-liner clearance	19	μM

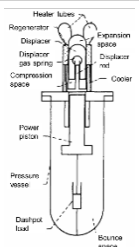
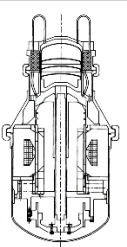
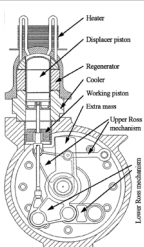
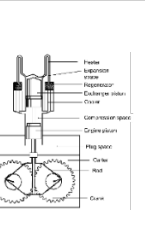
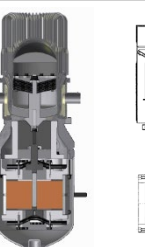
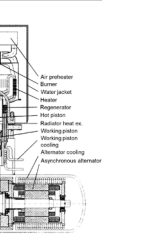
3. Range of the Design Parameters

3.1. Tubular Heat Exchanger Literature Review

To determine the range of the HHX design parameters, Table 2 shows the tube design parameters of several kilowatt Stirling engines employing tubular HHX developed by various institutions around the world. The design parameters of the tubular HHX are the tube inner diameter, tube length, and the number of tubes.

RE-1000 [24], a 1 kW-class FPSE developed in NASA’s Lewis facility in 1986, has an HHX consisting of 34 tubes whose inner diameter and length are ~2.4 mm and 183 mm, respectively. The SHARP (Stirling helium advanced reliable prototype) engine [28], 2 kW-class FPSE, was developed by Sunpower Inc. in 1989. The HHX of this engine is a tube type, and the inner diameter, length, and the number of tubes are 2.2 mm, 140 mm, and 60, respectively. The engine system was built by connecting two engine heads in parallel. These two engines produce 4 kW of electrical output, but the system electrical output is 3 kW, excluding the power consumption in the power requirements of the packaging (coolant pump, burner, battery charging). Thorsen [29] and Carlsen’s engines [30] are both crank-driven engines developed by the Technical University in Denmark, with an electrical output of 3 kW and 10 kW, respectively. The number of tubes in both engines is 24, which is relatively few compared to other engines. In particular, the tube inner diameter of Carlsen’s engine is 8 mm, which is more than twice that of other engines. The GPU-3 engine [31] is well known as a representative crank-driven Stirling engine, and its engine test results have been used as a reference to verify various crank-driven engine prediction models [32–34]. The 7 kW class Stirling engine developed by Qnergy Inc. is commercialized [35]; it is characterized by well-optimized configurations and component designs compared to the other prototype-level engines. Qnergy’s Stirling engine was presented by estimating the tube design parameters based on the released patent [31] because there was no data on which the design parameters were disclosed.

Table 2. Design parameters of HHX for several kilowatt-class Stirling engines from the literature.

Model or Author	#1. RE-1000 [24]	#2. SHARP [24]	#3. Thorsen [29]	#4. GPU-3 [31]	#5. QB-80 [35]	#6. Carlsen [30]	
Figure							
Power output, kW	1	2	3	4	7	10	
Type	free-piston	free-piston	kinematic	kinematic	free-piston	kinematic	
HHX parameter	Number of tubes	34	60	24	40	80	24
	Tube inner diameter, mm	2.36	2.2	3	3.02	3	8
	Tube length, mm	183	140	140	245.3	300	365

To summarize the range of tube parameters for all engines, as shown in Table 2, the tube inner diameter, number of tubes, and length are 2.2–8 mm, 24–80, and 140–365 mm, respectively. The tube parameter range in this study for optimizing the HHX design of the developed FPSE was determined by considering the shape of the developed FPSE while generally including the parameter ranges above. Each parameter was categorized into three levels, as presented in Table 3.

Table 3. Values of the design factors of the HHX.

Factor	Codes	Level Value		
		−1	0	1
Tube inner diameter (mm)	d_i	3	6	9
Tube length (mm)	l_t	100	200	300
Number of tubes	n_t	30	80	130

The characteristics of both objective functions are such that they offer greater brake power and efficiency of the engine. To find the optimal point-of-response values from the selected design factors, three-level design points were chosen for the three design variables, as shown in Table 4, using the central composite design (CCD). In addition to CCD, DOE that can be applied includes full factorial and Taguchi design. The efficient CCD method was used since the full factorial increases the analysis cases. Taguchi design is mainly used for the robust design that can minimize the influence of noise factors. Since the analysis model is used for the optimization of this paper, there is no need to consider the influence of noise factors, so the CCD method is used.

Table 4. HHX tube design set of central composite design (CCD).

Case	Tube Inner Diameter (mm)	Tube Length (mm)	Tube Number	Case	Tube Inner Diameter (mm)	Tube Length (mm)	Tube Number
case 1	3	100	30	case 9	6	300	80
case 2	3	300	30	case 10	6	200	130
case 3	3	200	80	case 11	9	100	30
case 4	3	100	130	case 12	9	300	30
case 5	3	300	130	case 13	9	200	80
case 6	6	200	30	case 14	9	100	130
case 7	6	100	80	case 15	9	300	130
case 8	6	200	80				

3.2. Design Constraints

Figure 2 shows the shape structure of the cylinder head and the heat exchanger tube. The cylinder head maintains the shape used in the previously developed engine. The HHX is U-shaped and is divided into an inner tube, an outer tube, and a bent tube. A number of tubes are arranged circumferentially in the cylinder head. The diameter of the outer tube array is fixed at 95 mm because it is a flow passage connected to the regenerator, and the diameter of the inner tube array changes according to the radius r_b of the bent tube. The tube length l_t is defined by Equation (1):

$$l_t = r_b\pi + 2b + a \quad (1)$$

where $a = -0.0084r_b^2 + 1.4684r_b + 1.4434$.

Here, b is the straight length of the inner tube and a is the length difference between the inner and outer tubes, which can be expressed as a second-order polynomial that increases with the length of r_b . For the tube bend radius r_b , a minimum value of 15 mm is required for production. The minimum value of the tube length determined as a design variable is 100 mm, meaning that the maximum value of r_b according to Equation (1) is approximately 25 mm when b is 0 mm.

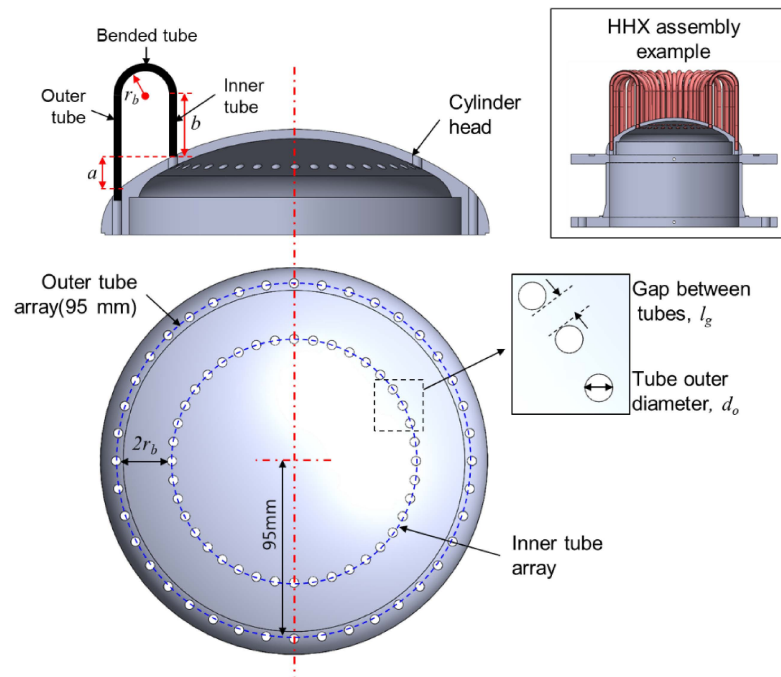


Figure 2. Shape structure of the cylinder head and the HHX tube.

In addition, the maximum number of applicable tubes varies according to the tube bend radius; this is determined by Equation (2) below:

$$n_{t,max} = 2\pi(95 - 2r_b) / (d_o + l_g) \tag{2}$$

where d_o is the outer diameter of the tube and l_g is the gap between the tubes. The tube thickness is fixed at 0.5 mm in consideration of the charge pressure of the engine, and the gap between the tubes remains at least 1 mm to simplify the machining of the holes.

Figure 3 shows the maximum applicable number of tubes according to the inner tube diameter and tube bending radius. As r_b increases, the number of tubes decreases for the same tube inner diameter. The maximum number of tubes that can be arranged in a given cylinder head shape is approximately 80, but the number of tubes here increases to 130 in order to identify the performance trend of the engine according to the number of tubes as well as the optimal design of the HHX.

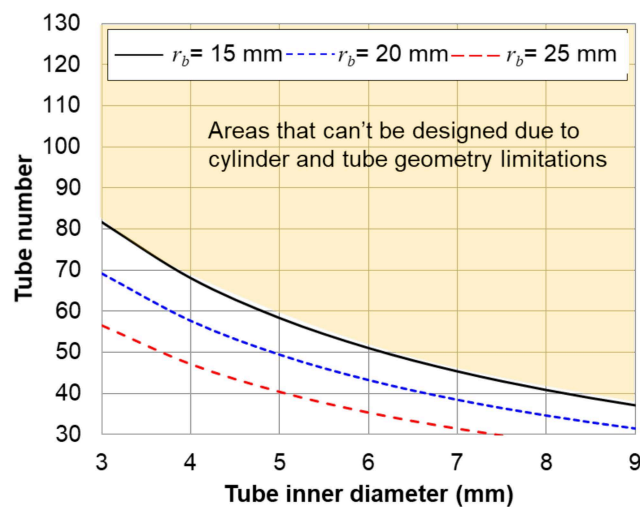


Figure 3. Maximum number of tubes applicable according to applicable tube inner diameter and tube bending radius.

4. Improved Quasi-Steady Flow (iQSF) Model

4.1. Modeling Procedure

The iQSF model is an improved model of a quasi-steady flow (QSF) model that is based on a second-order analysis [8], except for the regenerator part, where a third-order analysis is applied in iQSF to minimize errors by considering the effects of various losses in the analyses. In the iQSF model, the current FPSE can be largely divided into seven space cells: the wall of the cooler, the matrix of the regenerator, the wall of the heater, the expansion space, the bounce space for the displacer, the compression space, and the bounce space for the power piston. For the calculations of the thermodynamic characteristics of the system, appropriate assumptions were made for the heat transfer analyses. The working spaces including expansion and compression spaces were assumed to be adiabatic. The bounce spaces were modeled as closed systems with the assumption of an adiabatic process. In the heater and cooler regions, the heat addition to and rejection from the working fluid occur by forced convection under the isothermal wall temperature conditions. The regenerator is modeled as consecutive finite elements where convection heat transfer occurs between the matrix of the regenerator and the working fluid. The additional assumptions needed to solve the energy equations and to determine the performance of the FPSE are as follows:

1. The working fluid is considered an ideal gas.
2. Changes in the kinetic and potential energies are negligible.
3. The incompressible effect of the working fluid is negligible.
4. The mass of the working fluid inside the engine is constant.
5. All flows of the working fluid inside the engine are assumed to be periodic steady-state flows.
6. The motion of DP and PP follows a sinusoidal waveform with a constant velocity, amplitude, and phase.
7. The temperature distribution of the working fluid along the radial direction of the engine space is negligible.

Based on these assumptions, the governing equations and losses for each space cell of the engine were derived as shown in Tables 5 and 6, respectively, and were used for analyzing the thermodynamic characteristics of the FPSE by propagating the dynamics of one space cell to another.

The friction factor of the heat exchanger is based on Moody’s chart, and friction factor correlation equations ignoring the surface roughness are used [36]. In addition, the convective heat transfer coefficient was defined using the Reynolds analogy and the J-factor analogy, which are heat transfer correlation equations that depend on the Reynolds number in the pipe flow. The correlation equations of the heat exchanger are shown in Table 7 [36–38]. The friction coefficient and convective heat transfer coefficient of the regenerator were referenced from a study that experimentally measured the flow velocity, temperature, and pressure drop of the flow inside the regenerator [39]. The correlation equations of the regenerator are shown in Table 8.

Table 5. Governing equations of space cells for the iQSF model (here, $i = c, k, r, h, e$, and $j = p, d, rod$).

Space Cell	Governing Equations
Compression space	$\dot{H}_{sl,d} + \dot{H}_{sl,p} + \dot{H}_{sl,rod} - c_p \dot{m}_{ck} T_{ck} = \frac{c_p}{R} (\dot{p}_c V_c) + \frac{c_p}{R} (p_c \dot{V}_c)$
Expansion space	$-\dot{Q}_{sh} - \dot{Q}_{cond,d} - \dot{H}_{sl,d} + c_p \dot{m}_{he} T_{he} = \frac{c_p}{R} (\dot{p}_e V_e) + \frac{c_p}{R} (p_e \dot{V}_e)$
Heater	$\dot{Q}_h + c_p (\dot{m}_{rn,h} T_{rn,h} - \dot{m}_{he} T_{he}) = \frac{c_p}{R} (\dot{p}_h V_h)$
Regenerator	$\dot{Q}_{r1} - \dot{Q}_{reh1} + c_p (\dot{m}_{kr1} T_{kr1} - \dot{m}_{r1r2} T_{r1r2}) = \frac{c_p}{R} (\dot{p}_{r1} V_{r1})$
	\vdots
	$\dot{Q}_{rn} - \dot{Q}_{reh,n} + c_p (\dot{m}_{rn-1,rn} T_{rn-1,rn} - \dot{m}_{rn,h} T_{rn,h}) = \frac{c_p}{R} (\dot{p}_{rn} V_{rn})$
Cooler	$\dot{Q}_k + c_p (\dot{m}_{ck} T_{ck} - \dot{m}_{kr1} T_{kr1}) = \frac{c_p}{R} (\dot{p}_k V_k)$

Table 6. Definitions of losses and corresponding equations (here, $i = c, k, r, h, e$, and $j = p, d, rod$).

Losses		Equations
External heat losses	Structure conduction loss	$\dot{Q}_{cond,case} + \dot{Q}_{cond,cyl} = k_{case} \frac{A_{case}}{L_{case}} (T_{wh} - T_{wk}) + k_{cyl} \frac{A_{cyl}}{L_{cyl}} (T_{wh} - T_{wk})$
	Regenerator efficiency loss	$\dot{Q}_r = (1 - \epsilon) h_r A_{wt,r} (T_{wr} - T_r)$
Internal heat losses	Appendix gap loss	$\dot{Q}_{sh} + \dot{Q}_{cond,d} = \pi \frac{d_d}{2h_{gap}} k_{gas} X_d^2 \frac{(T_e - T_c)}{L_{app}} + k_d \frac{A_d}{L_d} (T_e - T_c)$
	leakage loss	$\dot{Q}_{sl,j} = \dot{m}_{sl,j} c_p (T_{in,j} - T_{out,j})$
Power losses	Seal friction loss	$\dot{W}_{sf,j} = -u_j \left[\frac{\mu L_{seal,j} \pi d_j u_j}{H_j} + \frac{\mu d_j h_j (p_{out,j} - p_{in,j})}{2} \right]$
	Flow friction loss	$\dot{Q}_{fr,i} = \Delta p_i A_{fr,i} \frac{\dot{g}_i}{\rho_i}$
	Gas spring hysteresis loss	$\dot{W}_{gsh} = \sqrt{\frac{1}{32} \omega \gamma^3 (\gamma - 1) T_w p k_{gas}} \left(\frac{\hat{V}_b}{V_b} \right)^2 A_{wt}$

Table 7. Correlation equations of the heat exchanger.

Model	Correlation
Rogers and Mayhew [36]	$Re \leq 2000,$ $f_f = 16Re^{-1}$
	$2000 < Re \leq 4000,$ $f_f = 7.343 \times 10^{-4} Re^{0.314}$
	$Re > 4000,$ $f_f = 0.0791 Re^{-0.25}$
Reynolds analogy [37,38] ($Re \leq 4000$)	$f_f = \frac{Re}{2} = Nu, h = \left \frac{1}{2} f_f Pr^{-1} g c_p \right $
Chilton-Colburn J-factor analogy [37,38] ($Re > 4000$)	$\frac{f_f}{2} = St Pr^{2/3}, h = \left \frac{1}{2} f_f Pr^{-2/3} g c_p \right $

Table 8. Correlation equations of the regenerator [39].

Flow Type	Oscillating Flow
Regenerator type	Woven wire (Stainless steel)
Wire diameter	0.05–0.23 mm
Porosity	0.645–0.754
Friction factor	$f_f = \frac{175}{Re} + 1.6$
Heat transfer coefficient	$Nu = 0.33 Re^{0.67}$

Structural conduction loss implies heat conduction loss through the external structure of the engine, specifically the engine case and the outer surface of the cylinder. The regenerator efficiency loss refers to the loss of thermal energy that cannot be reheated and is wasted during the reheating process of the regenerator. The appendix gap loss refers to the heat conduction loss through the gap and structure of the displacer and leakage loss implies the heat loss caused by the leakage of operating fluids. The seal friction loss and flow friction loss refer to losses caused by the viscous friction of the working fluid in the seal structure and caused while passing through the heat exchangers, respectively. The gas spring hysteresis loss refers to the loss due to the formation of hysteresis caused by the fluid viscosity distribution.

By integrating the governing equations and the losses, the pressure and temperature distribution in each space cell can be obtained, as shown in Figure 4, which also defines the

variables. Descriptions of the temperature and pressure distribution are given in detail in the references [8].

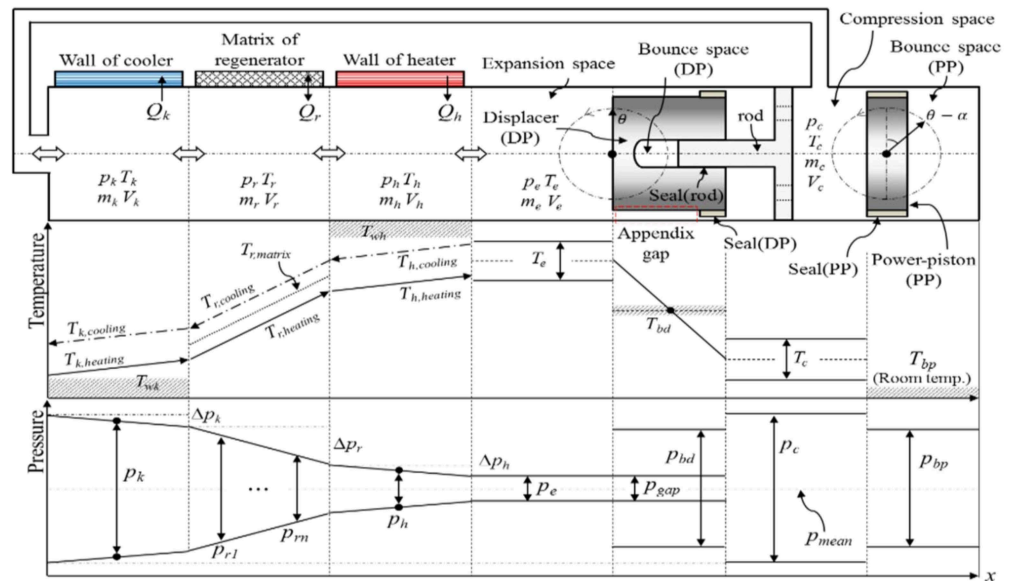


Figure 4. The thermodynamic system, temperature, and pressure levels of the FPSE.

Based on the quantity of state determined through the equations in Tables 5 and 6, the expansion work, compression work, and indicated power generated through the Stirling cycle are defined as follows:

$$\dot{W}_e = \oint p_e \frac{dV_e}{d\theta}, \dot{W}_c = \oint p_c \frac{dV_c}{d\theta} \tag{3}$$

$$P_{ind} = f(\dot{W}_e + \dot{W}_c) \tag{4}$$

Here, f is the operating frequency. The brake power applying the power losses, consisting of the gas spring hysteresis loss, heat exchanger friction loss, and seal friction loss, can be defined as the follows:

$$P_{brake} = P_{ind} - f \oint (\dot{W}_{gsh,j} + \dot{W}_{hxf,i} + \dot{W}_{sf,j}) d\theta \tag{5}$$

Based on this, the indicated efficiency and brake efficiency of the engine reflecting the heat conduction loss through the structure can be defined as follows:

$$\eta_{ind} = \frac{P_{ind}}{f \oint (\dot{Q}_h + \dot{Q}_{cond.case} + \dot{Q}_{cond.cyl}) d\theta} \tag{6}$$

$$\eta_{brake} = \frac{P_{brake}}{f \oint (\dot{Q}_h + \dot{Q}_{cond.case} + \dot{Q}_{cond.cyl}) d\theta} \tag{7}$$

4.2. Validity of the Model

For verification of the iQSF model, test result #1011 of the RE-1000 engine developed by NASA was used [24]. Test result #1011 is the standard experimental condition suggested in the literature, and the analytical models developed by many researchers were compared with the results of experiment #1011 [8,40]. The RE-1000 engine is a beta-type structure in which two pistons are located on the same axis, as shown in Figure 5. The DP and PP bounce spaces are connected to DP and PP, respectively, and act as a gas spring of the piston. The dashpot load acts as a mechanical load on PP. The heat exchanger consists of a

tube-type heater, a fin-type cooler, and a woven mesh-type regenerator. Table 9 shows the design parameters of RE-1000 and the operating conditions of #1011.

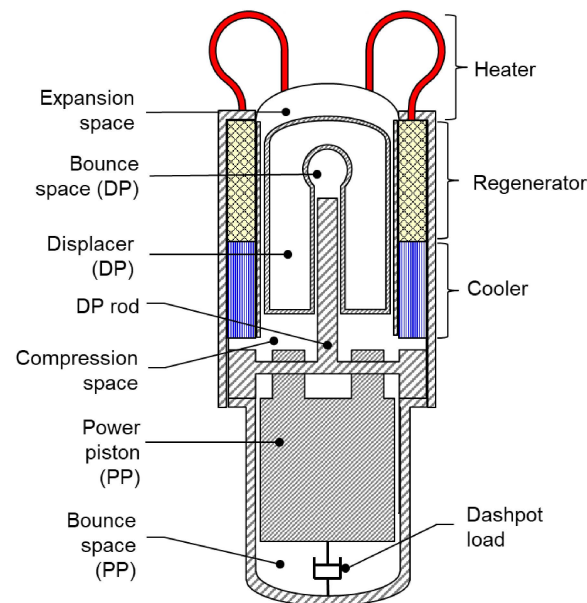


Figure 5. Schematic of the RE-1000 engine (built by NASA).

Table 9. Design parameters and operating conditions of the RE-1000 engine for the #1011 test.

Design Parameter		Value	Unit	Design Parameter		Value	Unit
Heater (tube type)	Number of tubes	34		DP	Diameter	56.4	mm
	Tube inner diameter	2.36	mm		Appendix gap clearance	0.381	mm
	Heater volume	27.33	cm ³		Seal clearance	0.033	mm
Cooler (fin type)	Fin number	135		DP rod	Diameter	16.7	mm
	Cooler volume	20.43	cm ³		Seal clearance	0.03	mm
Regenerator (woven mesh type)	Porosity	75.9	%	PP	Diameter	57.2	mm
	Wire diameter	0.0889	mm		Seal clearance	0.033	mm
	Void volume	56.37	cm ³		Heater temperature	600	°C
Space	Expansion space volume	27.74	cm ³	Operating condition	Cooler temperature	25	°C
	Compression space volume	54.8	cm ³		Charge pressure	70.6	bar
	DP bounce volume	30.79	cm ³		Frequency	30	Hz
	PP bounce volume	2615	cm ³		DP stroke	24.5	mm
Displacer	Diameter	56.4	mm	PP stroke	28	mm	
	Appendix gap clearance	0.381	mm	DP-PP phase angle	57.5	°	
	Seal clearance	0.033	mm				

Figure 6 shows a flow chart of the calculation process of the iQSF model. First, the engine design parameters and operating conditions serve as input. At this time, the step size of the iQSF model numerical analysis was determined to be one cycle per hundred cycles. The initial values of the iQSF model variables are determined, and numerical integration is conducted on the ordinary differential equations of the iQSF model using the fourth-order Runge–Kutta method. At this time, the analysis is repeated based on the convergence standard when the net heat transfer value of the regenerator during one cycle is less than 0.1% of the indicated output. The net heat transfer amount of the regenerator to zero during one cycle means that the Stirling cycle has reached a periodic steady state. At the same time, convergence is checked every one cycle, and in the absence of convergence, the initial value is reset and calculations are repeated to derive the result.

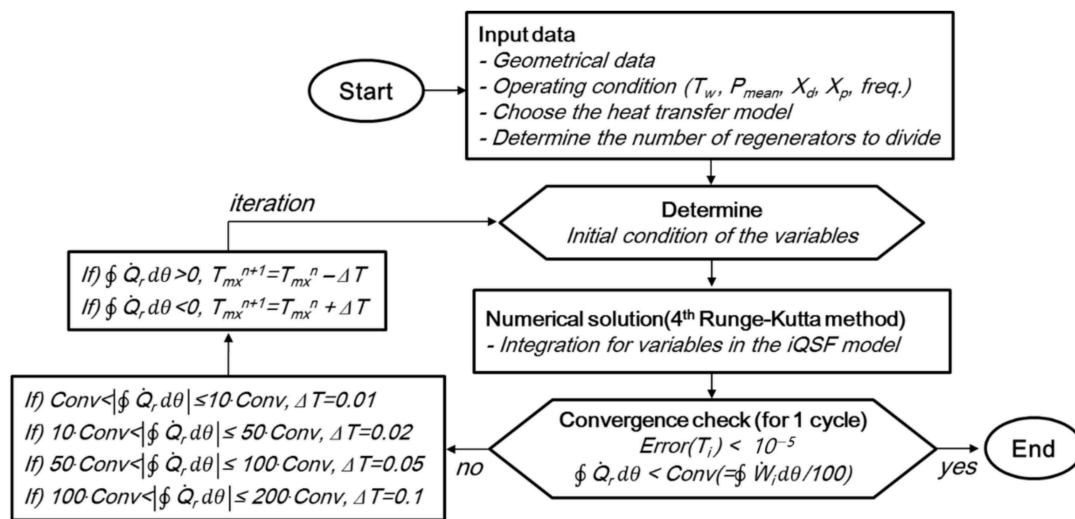


Figure 6. Flow chart of the calculation procedure of the iQSF model.

Figure 7 shows the predicted heat input and indicated power of the RE-1000 engine according to the number of finite elements when the regenerator space is divided into one-dimensional finite elements. As the number of the regenerator elements increases from 10 to 100, the heat input and the indicated power constantly converge from 7523 W to 4615 W and 1085 W to 1286 W, respectively. When the number of regenerator elements changed from 80 to 100, it was judged that the analysis results converged because the indicated power changed by less than 0.5%. Based on these results, all analyses were performed by dividing the regenerator space into 100 finite elements.

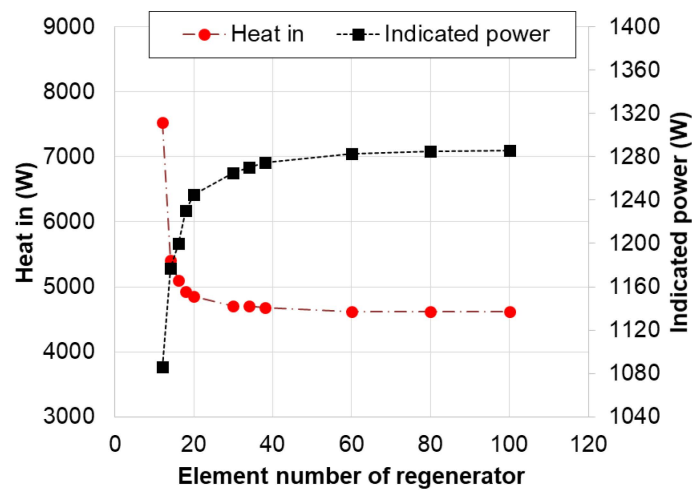


Figure 7. Predicted heat in and indicated power for the RE-1000 engine using the finite difference method (FDM) for the regenerator.

Figure 8 shows an energy flow diagram of the RE-1000 engine through the iQSF model analysis. The heat input is 4615 W, the heat including the loss of 3329 W is removed, and the indicated power of 1286 W is generated. The indicated power generates 1126 W of brake power, and the remaining 160 W is dissipated as power loss. The seal leakage loss is the largest, accounting for 55% of the total loss. This is presumed to be the cause of the large pressure difference between the engine space and the bounce space due to the high charge pressure. The heat exchanger friction loss occurs mostly in the regenerator with 60.5 W for the regenerator, 15.8 W for the heater, and 2.5 W for the cooler. The analysis found that a large amount of viscous friction arises due to the narrow flow passage of the regenerator.

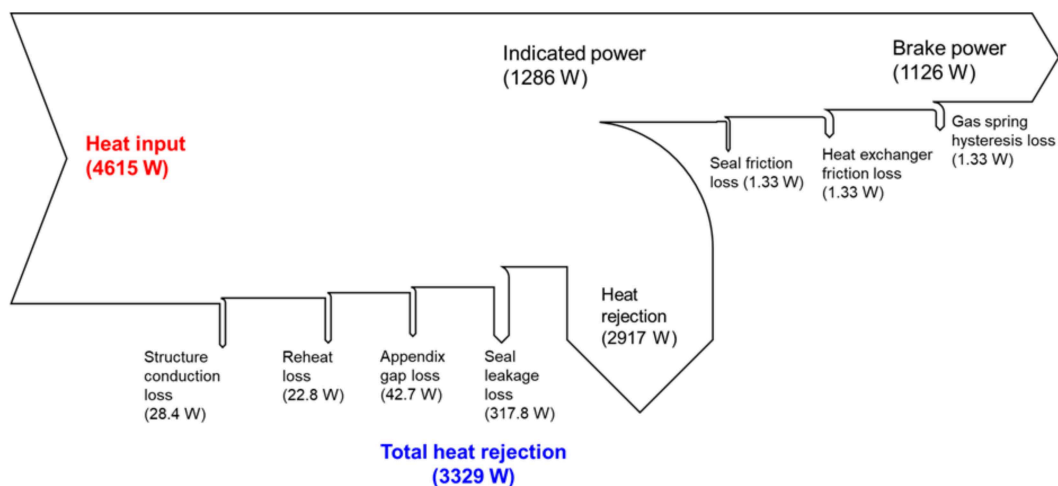


Figure 8. Energy flow of iQSF model for the RE-1000 engine.

Table 10 shows the prediction results of the Formosa model, the QSF model, and the iQSF model under identical RE-1000 test conditions [8,24,40]. First, the iQSF model predicts the test results with high accuracy compared to the existing QSF model. In particular, the predicted indicated power and efficiency of the iQSF model show high accuracy with less than 25% error compared to the test. In the Formosa results, the predicted indicated power showed a low error of 15.6% compared to the test results. However, the heat in and rejection outcomes are predicted with smaller values than those in the test results. The analysis shows that the Formosa model predicts the performance based on the idealized first-order analysis, which explains the lower predicted values compared to the test results.

Table 10. Comparison of various model results.

	Formosa Model [40]	QSF Model [8]	iQSF Model	Experiment (#1011) [24]
Heat in (W)	3777 (−6.46%)	4949.0 (22.6%)	4614.7 (14.3%)	4038
Heat rejection (W)	−2107 (−30.5%)	−2742.4 (−9.5%)	−3329.2 (9.8%)	−3032
Indicated power (W)	1100 (15.6%)	1717.4 (66.9%)	1286.8 (24.9%)	1030
Indicated efficiency (%)	29.2 (23.3%)	34.5 (35.3%)	27.9 (9.4%)	25.5

5. Regression Analysis

The results of the iQSF model analysis for the CCD case are listed in Table 11. Figure 9 shows effects of terms for (a) the brake power and (b) efficiency. The parameters with the strongest effects with regard to brake power and efficiency were the product of the tube's inner diameter (d_i) and the number of tubes (n_t); the p -value is less than 0.05, indicating a statistically significant effect on the brake power and efficiency. This is because $n_t \cdot d_i$ term is the factor that increases the dead volume the most. As a single term, performance is greatly affected in the order of n_t , d_i , and l_t . In particular, l_t has a relatively low effect on performance compared to n_t and d_i . The rest of the terms except for the $n_t \cdot d_i$ term also affect the performance, but the p -value is greater than 0.05, meaning that statistically, it is not considered to have a significant effect on the performance. However, in order to identify the performance trend according to the determined tube design parameters, the following regression models for the brake power and efficiency were established by considering all terms:

$$P_{brake}(W) = -2074 + 1776d_i + 2.6l_t + 89.2n_t - 102.5d_i^2 - 0.0498l_t^2 - 0.177n_t^2 + 1.76d_i \cdot l_t - 9.04d_i \cdot n_t + 0.046l_t \cdot n_t \quad (8)$$

$$\eta_{brake}(\%) = -10.54 + 9.59d_i - 0.009l_t + 0.445n_t - 0.504d_i^2 - 0.000159l_t^2 - 0.0009n_t^2 + 0.00555d_i \cdot l_t - 0.0451d_i \cdot n_t + 0.000167l_t \cdot n_t \quad (9)$$

Table 11. Results of the CCD case.

Case	Brake Power (W)	Brake Efficiency (%)	Case	Brake Power (W)	Brake Efficiency (%)
case 1	4639	22.71	case 9	7559	35.92
case 2	1350	7.53	case 10	7424	35.4
case 3	7157	33.4	case 11	6678	36.04
case 4	7967	38.7	case 12	7443	36.18
case 5	7543	35.52	case 13	6999	34.87
case 6	7691	37.44	case 14	6527	33.62
case 7	7446	38.24	case 15	6269	28.45
case 8	7657	36.86			

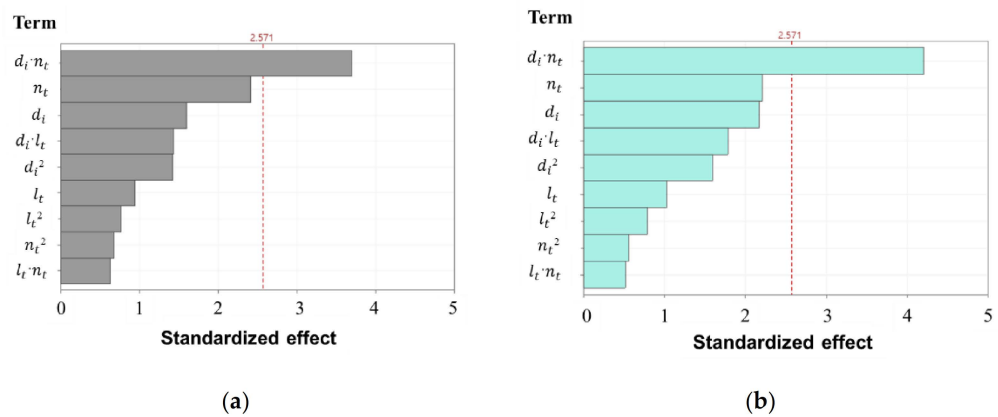


Figure 9. Effects of terms for (a) the brake power and (b) efficiency.

R-square represents the fitness of the regression model for the interpreted data. R-square for the indicated power and the efficiency calculated a high fit above 0.85.

6. Analysis of the Influence of Variables

We analyzed the effects of the design variables on (a) the brake power and (b) the efficiency, as shown in Figure 10. Comprehensively examining the effects of tube design parameters on the brake power and efficiency, the optimal value for the brake power and efficiency depends on the tube’s inner diameter. It is shown that when the tube’s inner diameter increases, the heat transfer area, which increases the performance, and the dead volume, which decreases the performance, increase simultaneously, forming an optimum value. An increase in the number of tubes significantly increases the heat transfer area compared to the dead volume, thus increasing both the brake power and the efficiency. As the tube length increases, the brake power finds its optimum value, but the efficiency decreases. This occurs because when the tube length increases, the heat transfer area increases, leading to the advantage of absorbing a considerable amount of heat. Thus, the brake power can increase, but the efficiency decreases because the friction loss increases.

Next, in order to identify the performance for the $n_t \cdot d_i$ term, which has the greatest influence on the brake power and efficiency, Figure 11 shows the predicted brake power and efficiency according to the inner tube diameter and the number of tubes using the regression model. Figure 11a shows the brake power for tube lengths of 100 mm, 200 mm, and 300 mm. Overall, the brake power increases when the tube inner diameter is small and with a high number of tubes, as this design can significantly increase the heat transfer area compared to the dead volume. Additionally, when both the tube inner diameter and the number of tubes are increased, the heat exchanger dead volume becomes very large and thus the brake power is reduced. The brake power increases in the order of tube lengths of 200 mm, 100 mm, and 300 mm; a similar trend is shown in Figure 10.

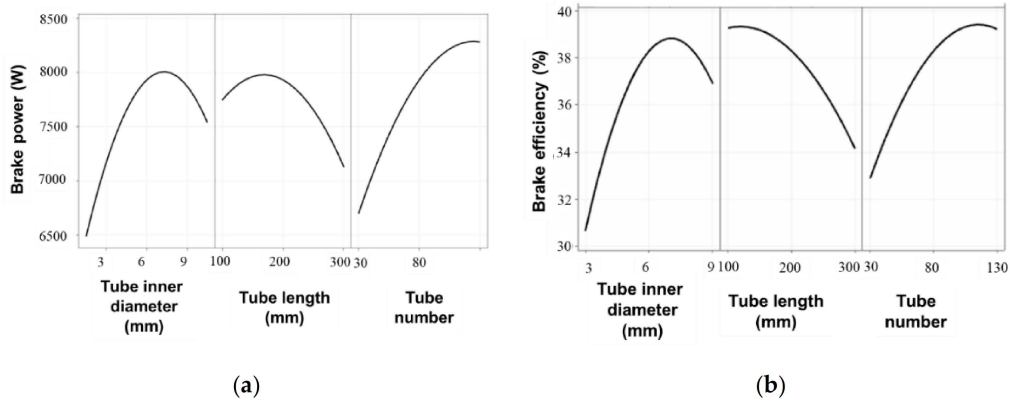


Figure 10. Variation of (a) the brake power and (b) brake efficiency according to the design factors of the tube inner diameter, tube length, and number of tubes.

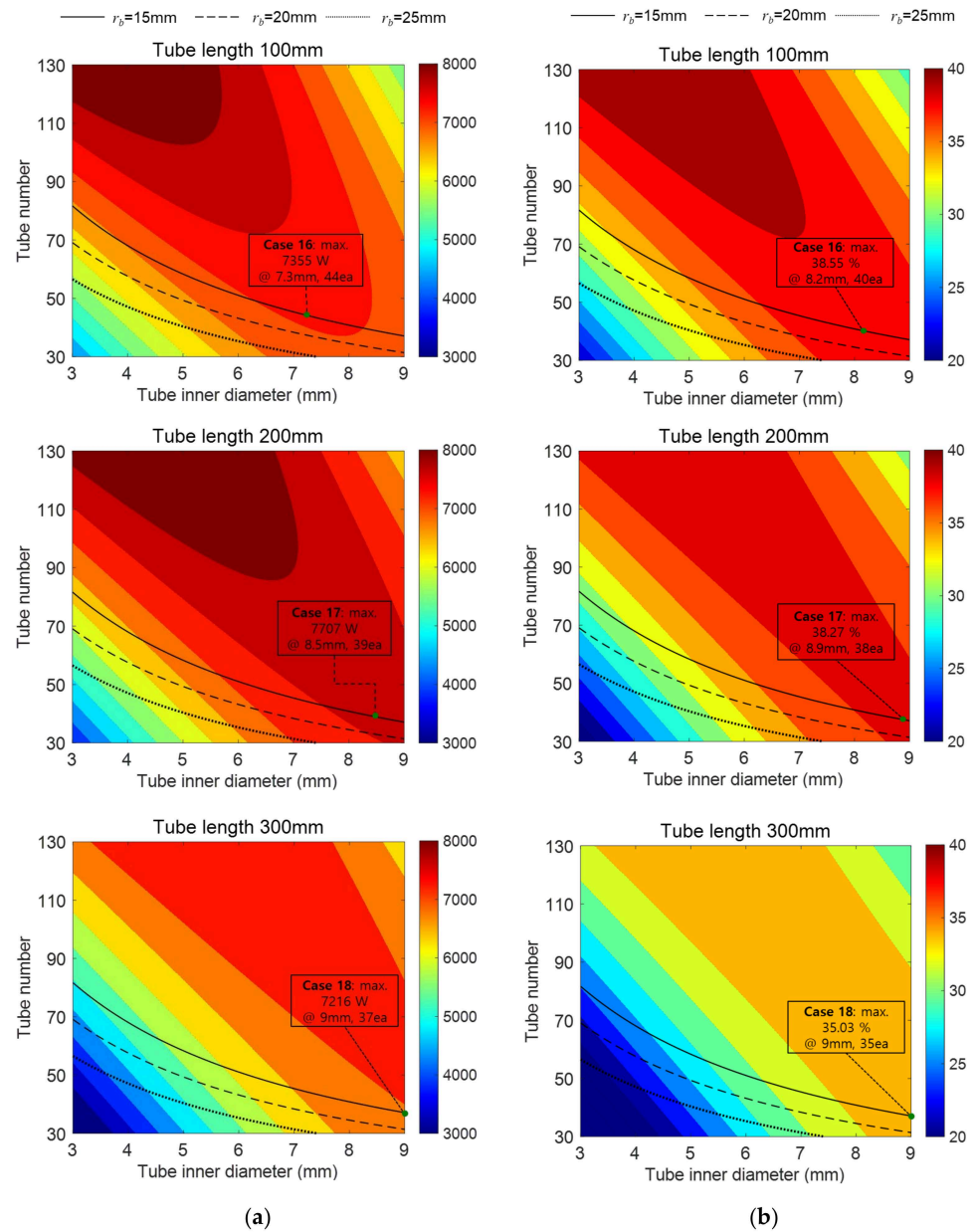


Figure 11. Predicted (a) brake power and (b) efficiency according to the inner tube diameter and the number of tubes using the regression model.

However, the realizable area in the cylinder structure is $r_b \leq 25$ mm. In all graphs in Figure 11, when r_b is 15 mm, 20 mm, and 25 mm, the realizable area is indicated by a line. In the graph showing a case with a tube length of 200 mm, the highest brake power of 7707 W (case 17) was predicted when the inner diameter of the tube was 8.5 mm and the number of tubes was 39.

Figure 11b shows the brake efficiency for tube lengths of 100 mm, 200 mm, and 300 mm. The brake efficiency trend according to the tube inner diameter and the number of tubes is similar to that of the brake power, but for the tube length, the maximum brake efficiency is shown at 100 mm, in contrast to the brake power result. With a limited r_b value, the highest possible efficiency is 38.55% (case 16), and the tube design parameters at this time are the tube inner diameter of 8.2 mm, number of tubes of 40, and tube length of 100 mm.

The tube inner diameter and the number of tubes that generate maximum brake power and efficiency are very similar at about ~8.5 mm and ~39, respectively, while the tube length is different at 100 mm and 200 mm, respectively. Because the tube length can change freely under the limited r_b design condition, design optimization for the tube length was performed through an iQSF analysis.

Figure 12 shows (a) the brake output and (b) efficiency with respect to changes in the tube length when the tube inner diameter is 8.5 mm and the number of tubes is 39 through the iQSF analysis. The brake efficiency has slight fluctuations in value due to numerical error; thus, a clear trend was confirmed through a cubic polynomial fitting line. First, looking at the brake power, when the tube length is 200 mm, the result of the iQSF analysis was approximately 7400 W, but in the regression model, the brake power is 7707 W, which causes a discrepancy of about 4%, stemming from the error of the regression model. As mentioned above, because the R-squared of the regression model is about 0.9, there may be an error of 10% or less. The brake efficiency also has a regression error of less than 10%. The brake power calculated through the iQSF analysis is the highest at a tube length of 260 mm, and the brake efficiency rate is the highest at a tube length of 180 mm. The brake power variation was nearly identical within 0.3% in the tube length range of 220–320 mm, and the brake efficiency variation was similar within 0.5% in the tube length range of 140–220 mm, meaning that the tube length was set to 220 mm, which can increase both the output and the efficiency. Finally, the tube inner diameter, tube length, and the number of tubes were determined to be 8.5 mm, 220 mm, and 39 tubes, respectively. The optimal design condition is defined as case 19.

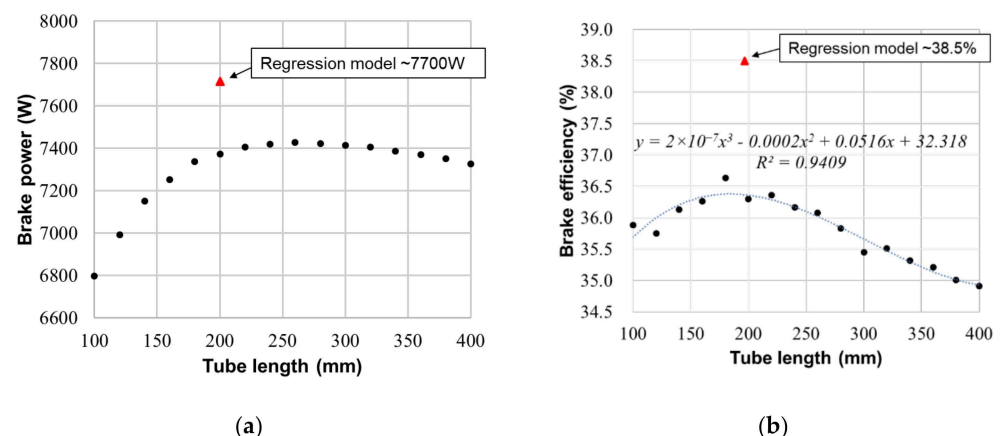


Figure 12. Predicted (a) brake power and (b) efficiency with respect to tube length changes when the tube inner diameter is 8.5 mm and the number of tubes is 39 through the iQSF model.

7. Loss Analysis for the Tube Design Parameters

Figure 13 shows the portion of the total loss for the optimal HHX design conditions (inner tube diameter 8.5 mm, tube length 220 mm, number of tubes 39) in the optimal case 19 determined above. The regenerator efficiency loss accounted for the largest portion

at 42.3%, followed by the appendix gap loss and DP seal leakage loss at 28.1% and 14.6%, respectively. This generally shows values similar to those of the parasitic loss of a well-designed Stirling engine [8].

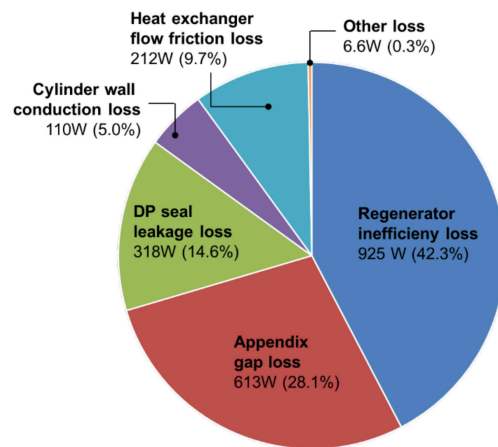


Figure 13. Portion of the total loss for the optimal HHX design conditions in the optimal case 19 (inner tube diameter 8.5 mm, tube length 220 mm, number of tubes 39).

Figure 14 shows both the major loss for the design condition that generates the maximum brake power for cases 16, 17, and 18 in Figure 11 and the major loss in the worst case 2 with the lowest brake power in Table 11. The major losses are the DP seal leakage loss, heat exchanger flow friction loss, regenerator efficiency loss, and appendix gap loss, and the remaining losses are not indicated due to their small values. The tube inner diameter and the number of tubes for the worst case are 3 mm and 30, respectively, lower than in other cases, meaning that the flow friction loss generated inside the HHX is very high at approximately 3500 W. Among the input parameters of the iQSF analysis, two pistons motions operate under a fixed condition such that the volume flow rate of all cases is identical, whereas the flow area inside the HHX is very narrow, resulting in a large flow friction loss due to the high gas flow rate. Moreover, as the flow resistance that arises when the working gas moves from the expansion space to the HHX space increases, the flow rate of the working gas delivered to the compression space through the DP gap also increases. Accordingly, the DP seal leakage loss is also very high at approximately 7500 W. As a result, the flow rate of the working gas through the regenerator is reduced such that the regenerator inefficiency loss is relatively small compared to the other cases. The other three design conditions are similar in terms of the magnitude of the major losses due to the well-designed HHX.

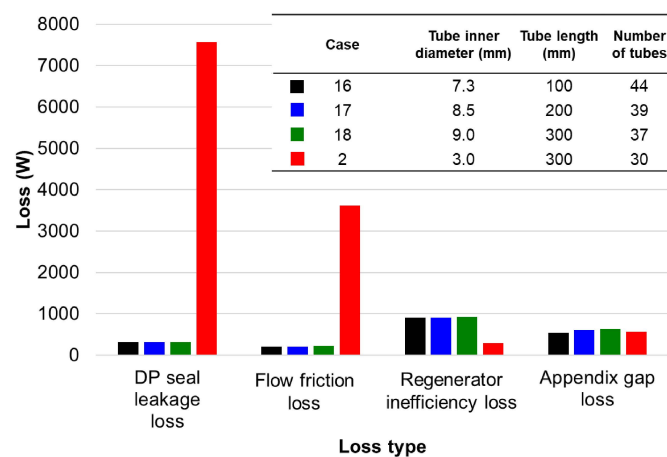


Figure 14. Major loss for the design condition that generates the maximum brake power for cases 16, 17, and 18 in Figure 11 and the major loss in the worst case 2 with the lowest brake power in Table 11.

8. Conclusions

This paper presents the development and verification of an improved quasi-steady flow (iQSF) model and undertakes design optimization of the heat exchanger of the FPSE developed by Nexergy lab at Seoultech using the iQSF model.

The iQSF model additionally applied heat losses and power losses based on the QSF model. In addition, the heat transfer model of the oscillating flow condition, which is the flow of the working fluid in an actual Stirling engine, was applied, and FDM was applied to the regenerator space to improve the prediction of the internal flow of the regenerator. Model verification was performed using the experimental results of the RE-1000 engine, an FPSE developed by Sunpower. The iQSF model significantly improved the model prediction error from 66.9 to 24.9% compared to the existing QSF model.

In order to optimize the design of the HHX of the engine developed by our institution using the iQSF model, the selected design factors of the HHX were the tube inner diameter, the tube length, and the number of tubes, and the design range was determined through a literature review of kilowatt Stirling engines. To find the optimal point-of-response values from the selected design factor, the HHX design set of CCD was constructed and the brake power and efficiency were predicted through the iQSF model. The parameters with the greatest effects on the brake power and efficiency were the product of the tube inner diameter and the number of tubes, and single factors that affected the performance were the number of tubes, tube inner diameter, and tube length in that order.

To optimize the HHX design, using the regression model derived from response surface regression, the inner diameter and number of tubes with the highest brake power and efficiency were determined to be 8.5 mm and 39, respectively. The tube length with high design freedom was determined to be 220 mm using the iQSF model. As a result, the brake power and efficiency of the FPSE with the optimized HHX were predicted to be 7.4 kW and 36.4%, respectively, through the iQSF model.

Finally, the major losses of three cases with good performance and the worst cases were analyzed through the iQSF model. It was confirmed that as the inner diameter and number of tubes decreased, the flow resistance increased such that not only the flow friction loss but also the DP seal leakage loss increased significantly. Through this, it was confirmed that the flow friction loss and the DP seal leakage loss are very important design considerations in the design of the HHX of the FPSE.

A limitation of the iQSF model used in this paper is that the piston motion must be constrained. The iQSF model is suitable for use in a mechanical type Stirling engine in which the piston motion is fixed, but there is a limit to using it in the FPSE in which the piston motion is changed. Therefore, in the future, we plan to develop a model that can predict the piston motion by combining the iQSF model and the equation of motion of the piston of the FPSE.

Author Contributions: Conceptualization, K.S.; methodology, K.S. and T.Y.K.; software, D.-J.K. and Y.P.; validation, D.-J.K. and Y.P.; formal analysis, D.-J.K.; investigation, D.-J.K. and T.Y.K.; writing—original draft preparation, D.-J.K. and T.Y.K.; writing—review and editing, D.-J.K.; supervision, K.S. All authors have read and agreed to the published version of the manuscript.

Funding: This research was supported by the National Research Foundation of Korea (NRF) funded by the Ministry of Science, ICT (NRF-2018R1D1A1B07047868).

Institutional Review Board Statement: Not applicable.

Informed Consent Statement: Not applicable.

Data Availability Statement: Not applicable.

Conflicts of Interest: The authors declare no conflict of interest.

Abbreviations

Symbols

A	area [m ²]
A_{wt}	wetted area [m ²]
a	length difference between the inner and outer tubes [m]
b	straight length of the inner tube [m]
c_p	specific heat at constant pressure [J/kg·K]
c_v	specific heat at constant volume [J/kg·K]
d	hydraulic diameter [m]
d_i	tube inner diameter [m]
d_o	tube outer diameter [m]
f	operating frequency [Hz]
f_f	fanning friction factor
g	mass flux [kg/m ² ·s]
H	enthalpy [J]
h	convective heat transfer coefficient [W/m ² ·K]
k	thermal conductivity [W/m·K]
L	length [m]
l_t	tube length [m]
m	mass [kg]
Nu	Nusselt number
n_t	Number of tubes
P	power [W]
p	pressure [Pa]
Q	heat [J]
R	gas constant [J/kg·K]
Re	Reynolds number
r_b	radius of the bent tube [m]
St	Stanton number
T	temperature [K]
T_w	wall temperature [K]
t	time [s]
u	gas velocity [m/s]
V	volume [m ³]
W	work [J]
X	amplitude [m]

Greek letters

γ	specific heat ratio
ε	effectiveness
η	efficiency
θ	crank angle [°]
κ	thermal conductivity [W/m·K]
μ	viscosity [Pa·s]

Subscripts

app	appendix gap
b	bounce space
c	compression space
ck	compression space to cooler space
$cond$	conduction
cyl	cylinder
d	displacer
e	expansion space
fr	free flow
gsh	gas spring hysteresis
h	heater
he	heater space to expansion space
hx	heat exchanger friction

<i>ind</i>	indicated
<i>k</i>	cooler
<i>kr</i>	cooler space to regenerator space
<i>p</i>	power piston
<i>r</i>	regenerator
<i>reh</i>	reheat
<i>sh</i>	shuttle
<i>sl</i>	seal leakage
<i>wh</i>	heater wall
<i>wk</i>	cooler wall

References

- Jackson, J. Ensuring emergency power for critical municipal services with natural gas-fired combined heat and power (CHP) systems: A cost-benefit analysis of a preemptive strategy. *Energy Policy* **2007**, *35*, 5931–5937. [[CrossRef](#)]
- Beale, W.T. *Free Piston Stirling Engines—Some Model Tests and Simulations*; 0148-7191, SAE Technical Paper; SAE: Warrendale, PA, USA, 1969.
- Beale, W.T. Stirling Cycle Type Thermal Device. U.S. Patent US3552120A, 5 January 1971.
- Dyson, R.; Wilson, S.; Tew, R. Review of computational stirling analysis methods. In Proceedings of the 2nd International Energy Conversion Engineering Conference, Providence, RI, USA, 16–19 August 2004; p. 5582.
- Walker, G.; Senft, J.R. *Free Piston Stirling Engines*; Springer: Berlin/Heidelberg, Germany, 1985.
- Schmidt, G. The theory of Lehmann's calorimetric machine. *Z. Des Ver. Dtsch. Ing.* **1871**, *15*, 98–112.
- Finkelstein, T. *Generalized Thermodynamic Analysis of Stirling Engines*; 0148-7191, SAE Technical Paper; SAE: Warrendale, PA, USA, 1960.
- Urieli, I.; Berchowitz, D.M. *Stirling Cycle Engine Analysis*; Taylor & Francis: Boca Raton, FL, USA, 1984.
- Parlak, N.; Wagner, A.; Elsner, M.; Soyhan, H.S. Thermodynamic analysis of a gamma type Stirling engine in non-ideal adiabatic conditions. *Renew. Energy* **2009**, *34*, 266–273. [[CrossRef](#)]
- Babaelahi, M.; Sayyaadi, H. Simple-II: A new numerical thermal model for predicting thermal performance of Stirling engines. *Energy* **2014**, *69*, 873–890. [[CrossRef](#)]
- Hosseinzade, H.; Sayyaadi, H. CAFS: The Combined Adiabatic-Finite Speed thermal model for simulation and optimization of Stirling engines. *Energy Convers. Manag.* **2015**, *91*, 32–53. [[CrossRef](#)]
- Sowale, A.; Anthony, E.J.; Kolios, A.J. Optimisation of a quasi-steady model of a free-piston stirling engine. *Energies* **2019**, *12*, 72. [[CrossRef](#)]
- Torres García, M.; Carvajal Trujillo, E.; Vélez Godiño, J.A.; Sánchez Martínez, D. Thermodynamic model for performance analysis of a Stirling engine prototype. *Energies* **2018**, *11*, 2655. [[CrossRef](#)]
- Finkelstein, T. Computer analysis of Stirling engines. *Advances in Cryogenic Engineering. Adv. Cryogenic Eng.* **1975**, *20*, 269–282.
- Urieli, I.; Rallis, C.J.; Berchowitz, D.M. Computer simulation of Stirling cycle machines. In Proceedings of the 12th Intersociety Energy Conversion Engineering Conference, Washington, DC, USA, 28 August–2 September 1977; pp. 1512–1521.
- Berchowitz, D.M.; Rallis, C. A computer and experimental simulation of stirling cycle machines. In Proceedings of the 13th Intersociety Energy Conversion Engineering Conference, San Diego, CA, USA, 20–25 August 1978; pp. 1730–1738.
- Gedeon, D. Sage-Object-oriented software for Stirling machine design. In Proceedings of the Intersociety Energy Conversion Engineering Conference, Monterey, CA, USA, 7–12 August 1994; p. 4106.
- Gedeon, D. *Sage Stirling-Cycle Model-Class Reference Guide*; Gedeon Associates: Athens, OH, USA, 1999; p. 16922.
- Gedeon, D. *Sage User's Guide*; Gedeon Associates: Athens, OH, USA, 2009; p. 16922.
- Mahkamov, K.; Djumanov, D. Three-dimensional CFD modeling of a Stirling engine. In Proceedings of the 11th International Stirling Engine Conference, Rome, Italy, 19–21 November 2003; pp. 97–107.
- Ibrahim, M.B.; Zhang, Z.-G.; Tew, R.C., Jr.; Gedeon, D.; Simon, T.W. CFD modeling of free-piston Stirling engines. In Proceedings of the 36th Intersociety Energy Conversion Engineering Conference, Savannah, GA, USA, 29 July–2 August 2001.
- Wilson, S.; Dyson, R.; Tew, R.; Ibrahim, M. Multi-D CFD Modeling of Free-Piston Stirling Converter at NASA GRC. In Proceedings of the 2nd International Energy Conversion Engineering Conference, Providence, RI, USA, 16–19 August 2004; p. 5673.
- Lee, K.-S.; Lee, S.-H.; Park, J.-H.; Choi, J.-Y.; Sim, K.-H. Design and experimental analysis of a 3 kW single-phase linear permanent magnet generator for stirling engines. *IEEE Trans. Magn.* **2018**, *54*, 1–5. [[CrossRef](#)]
- Schreiber, J.G.; Geng, S.M.; Lorenz, G.V. *Re-1000 Free-Piston Stirling Engine Sensitivity Test Results*; National Aeronautics and Space Administration Report; National Aeronautics and Space Administration: Washington, DC, USA, 1986.
- Khamneh, M.E.; Askari-Paykani, M.; Shahverdi, H.; Hadavi, S.M.M.; Emami, M. Optimization of spring-back in creep age forming process of 7075 Al-Alclad alloy using D-optimal design of experiment method. *Measurement* **2016**, *88*, 278–286. [[CrossRef](#)]
- Kanlayasiri, K.; Boonmung, S. Effects of wire-EDM machining variables on surface roughness of newly developed DC 53 die steel: Design of experiments and regression model. *J. Mater. Process. Technol.* **2007**, *192*, 459–464. [[CrossRef](#)]
- Lee, C.-W.; Kim, D.-J.; Kim, S.-K.; Sim, K.-H. Design Optimization of Flexure Springs for Free-Piston Stirling Engines and Experimental Evaluations with Fatigue Testing. *Energies* **2021**, *14*, 5156. [[CrossRef](#)]

28. Lane, N.; Berchowitz, D.; Shade, D.; Karandikar, A. Development of a high frequency Stirling engine-powered 3 kW (e) generator set. In Proceedings of the 24th Intersociety Energy Conversion Engineering Conference, Washington, DC, USA, 6–11 August 1989; pp. 2213–2218.
29. Thorsen, J.E.; Bovin, J.; Carlsen, H. 3 kW Stirling engine for power and heat production. In Proceedings of the IECEC 96—31st Intersociety Energy Conversion Engineering Conference, Washington, DC, USA, 11–16 August 1996; Volume 1282, pp. 1289–1294.
30. Carlsen, H. Operating experience with a 10 kW hermetic Stirling Engine. In Proceedings of the Intersociety Energy Conversion Engineering Conference, Monterey, CA, USA, 7–12 August 1994; p. 3802.
31. Timoumi, Y.; Tlili, I.; Nasrallah, S.B. Design and performance optimization of GPU-3 Stirling engines. *Energy* **2008**, *33*, 1100–1114. [[CrossRef](#)]
32. Formosa, F.; Despesse, G. Analytical model for Stirling cycle machine design. *Energy Convers. Manag.* **2010**, *51*, 1855–1863. [[CrossRef](#)]
33. Babaelahi, M.; Sayyaadi, H. Analytical closed-form model for predicting the power and efficiency of Stirling engines based on a comprehensive numerical model and the genetic programming. *Energy* **2016**, *98*, 324–339. [[CrossRef](#)]
34. Ahmed, F.; Hulin, H.; Khan, A.M. Numerical modeling and optimization of beta-type Stirling engine. *Appl. Therm. Eng.* **2019**, *149*, 385–400. [[CrossRef](#)]
35. Augenblick, J.E.; McFadden, G.D.; Peterson, A.A.; Rink, K.K. Tubular Heat Exchange. U.S. Patent US206355A, 15 August 2013.
36. Rogers, G.F.C.; Mayhew, Y.R. *Engineering Thermodynamics, Work and Heat Transfer*; Longman Scientific: Harlow, UK, 1992.
37. Incropera, F.P.; DeWitt, D.P.; Bergman, T.L.; Lavine, A.S. *Fundamentals of Heat and Mass Transfer*; Wiley: New York, NY, USA, 1996; Volume 6.
38. Geankoplis, C.J. *Transport Processes and Separation Process Principles*, 4th ed.; Person Education: London, UK, 2003.
39. Tanaka, M.; Yamashita, I.; Chisaka, F. Flow and heat transfer characteristics of the Stirling engine regenerator in an oscillating flow. Ser. 2, Fluids engineering, heat transfer, power, combustion, thermophysical properties. *JSME Int. J.* **1990**, *33*, 283–289.
40. Formosa, F. Coupled thermodynamic–dynamic semi-analytical model of free piston Stirling engines. *Energy Convers. Manag.* **2011**, *52*, 2098–2109. [[CrossRef](#)]